Residual-stress Determination by Single-axis Holographic Interferometry and Hole Drilling—Part I: Theory

by A. Makino and D. Nelson

ABSTRACT—A method is described for the rapid, accurate determination of residual stresses from a holographic interference fringe pattern. The pattern is generated by the displacement field caused by localized relief of residual stresses via the introduction of a small, shallow hole into the surface of a component or test specimen. The theoretical development of the holographic method is summarized. An example is given showing how the method can be applied to a typical experimentally observed fringe pattern to determine principal residual stresses and directions.

List of Symbols

$\tilde{a}$, $\tilde{b}$, $\tilde{c}$ = nondimensional coefficients derived from $\tilde{A}$, $\tilde{B}$, $\tilde{C}$
h = depth of a blind hole
n = fringe order
n^0 = fringe order in a fringe pattern that does not include out-of-plane displacements
$n^{(1)}$, $n^{(1')}$ = fringe orders at diametrically opposite points around a hole
$n^{(i)}$, $n^{(i')}$ = fringe orders at diametrically opposite points around a hole
r = radial coordinate
r_0 = radius of a blind hole
t = specimen thickness
u_x, u_y, u_z = displacement components in a Cartesian coordinate system
u_r, u_θ, u_z = displacement components in a cylindrical coordinate system
z_{vp} = z-coordinate of the observer's position
$\tilde{A}$, $\tilde{B}$, $\tilde{C}$ = coefficients in the expressions for the displacement field [eq (2)]
C_{ij} = elements of the matrix of coefficients in eqs (19) and (21)
D = diameter of a blind hole
E = Young's modulus
K_x, K_y, K_z = Cartesian components of the sensitivity vector
K_x^0, K_y^0, K_z^0 = Cartesian components of the sensitivity vector when the observer is at infinity
$\tilde{e}_x$, $\tilde{e}_y$, $\tilde{e}_z$ = unit vectors in a Cartesian coordinate system
$\tilde{k}_1$ = propagation vector in the illumination direction
$\tilde{k}_2$ = propagation vector in the viewing direction
$\tilde{u}$ = displacement vector
$\tilde{K}$ = sensitivity vector
$\tilde{K}^0$ = sensitivity vector when the observer is at infinity
α = angle defined by $\tan^{-1}(r/z_{vp})$
β = orientation of the principal axes
γ_1 = grazing angle of illumination
ζ = inclination of the illumination direction
θ = circumferential coordinate in a cylindrical coordinate system
λ = wavelength of the illumination source
ν = Poisson's ratio
ρ = ratio of hole radius to radial coordinate (r_0/r)
σ_{xx}, σ_{yy}, τ_{xy} = components of the stress tensor (Cartesian coordinate system)
σ_1, σ_2 = principal stresses
ϕ = phase shift
$\phi(x, y)$, $\phi(r, \theta)$ = fringe function

A. Makino (SEM Member) is Research Assistant, and D. Nelson (SEM Member) is Associate Professor, Stanford University, Mechanical Engineering Department, M/C 4021, Stanford, CA 94305-4021.

Original manuscript submitted: March, 1992. Final manuscript received: June 4, 1993.

Φ_0 = net phase shift of the object beam
Φ_R = net phase shift of the reference beam
$\Delta\Phi$ = net phase shift change

Introduction

The blind-hole drilling technique utilizing strain-gage rosettes[1,2] is a widely applied method for determining residual stresses, but it has certain disadvantages, including: (a) the time and costs associated with installing a special rosette and precision drilling guide at each measurement location, (b) the necessity that the location be sufficiently large and flat enough to accommodate a rosette and its drilling guide, (c) inaccuracies introduced by holes drilled even slightly off-center in a rosette or by apparent strains induced by temperature fluctuations, unless properly taken into account, and (d) inapplicability of conventional rosettes in hostile environments (e.g., elevated temperatures).

During the 1980s, the possibility of determining residual stresses through use of optical techniques in conjunction with hole drilling was explored by a number of researchers. In essence, the optical techniques were intended to replace strain rosettes by furnishing information on surface displacements produced by hole drilling, from which residual stresses could be deduced, at least in principle.

The use of moiré interferometry as an optical technique for relating the in-plane displacements from hole drilling to residual stresses was proposed by McDonach *et al.*[3] and has been further developed by Nicoletto[4,5] for those cases where the in-plane displacements can be described by closed form, plane-stress formulations (e.g., through holes in thin plates). For blind holes, Furgiuele *et al.*[6] have used numerical analyses to develop relations between in-plane displacements and stresses. Use of a moiré grating in place of a strain rosette eliminates some of the drawbacks associated with rosettes. However installation of a grating can still be somewhat time consuming and is limited to structural regions and environments receptive to gratings.

Other optical methods such as shearography have been applied with surface indentations[7] instead of hole drilling but they are qualitative rather than quantitative in their present state.

To avoid some of the limitations associated with rosettes and gratings, the feasibility of using holographic interferometry as an optical technique for providing information about surface displacements from hole drilling was shown independently at about the same time by Antonov,[8] Bass *et al.*,[9] and Nelson and McCrickerd.[10] Antonov proposed that the out-of-plane displacements from hole drilling could be used to determine residual stresses for through holes in thin sheets. Since out-of-plane displacements from hole drilling are considerably smaller than those from in-plane displacements, the sensitivity of the approach is correspondingly reduced. Bass *et al.* predicted optical interference fringe patterns for holes drilled into rock masses assuming that different states of stress and stress levels were applied to the rock. Stresses were deduced by trying to match predicted patterns with experimentally observed ones. Refinements of the same technique are reported by Smither *et al.*[11,12] Extensive descriptions of geophysical applications of holography can be found in Ref. 13. Nelson and McCrickerd[10] proposed a fringe counting method that might be used to quickly convert the displacement information contained in an observed fringe pattern to estimates of residual stresses but offered no theoretical derivation for the approach.

This paper is divided into two parts. The first provides a theoretical derivation of a generalized fringe-counting method for determining residual stresses from holographic/hole drilling tests and an example of how the method can be applied to a typical fringe pattern. The second part, Ref. 14, describes experiments used to generate fringe patterns and provides a more extensive comparison of predictions of residual stress from the fringe counting method with experimental results.

The approach described in this paper was developed with the following criteria in mind: (a) that it require only one hologram per measurement location, made with a single beam and direction of illumination, (b) that it be able to process the displacement information contained in an optical interference fringe pattern and convert it to estimates of stress in a way that is relatively easy to learn and implement, and (c) that it produce reasonable estimates of stress even if the illumination direction does not coincide with the direction of maximum principal stress, since knowledge of that direction may not be known in advance of testing.

Displacement Relations for a Hole Drilled in a Uniform Residual-stress Field

The introduction of a hole in a previously stressed material produces a displacement field which can be found from the difference between two known stress solutions.[15] Assuming a plane-stress state characterized by σ_{xx}, σ_{yy}, τ_{xy}, which remain uniform over a thin plate, as shown in Fig. 1, the displacement field produced by drilling a through hole of radius r_0 can be expressed in cylindrical coordinates as

$$u_r = \frac{r_0}{2E}\{(1+\nu)(\sigma_{xx}+\sigma_{yy})\rho + [(\sigma_{xx}-\sigma_{yy})\cos 2\theta + 2\tau_{xy}\sin 2\theta][4\rho - (1+\nu)\rho^3]\}$$

$$u_\theta = -\frac{r_0}{2E}\{[(\sigma_{xx}-\sigma_{yy})\sin 2\theta - 2\tau_{xy}\cos 2\theta] \cdot [2(1-\nu)\rho + (1+\nu)\rho^2]\}$$

$$u_z = \frac{\nu t}{E}\rho^2[(\sigma_{xx}-\sigma_{yy})\cos 2\theta + 2\tau_{xy}\sin 2\theta] \quad (1)$$

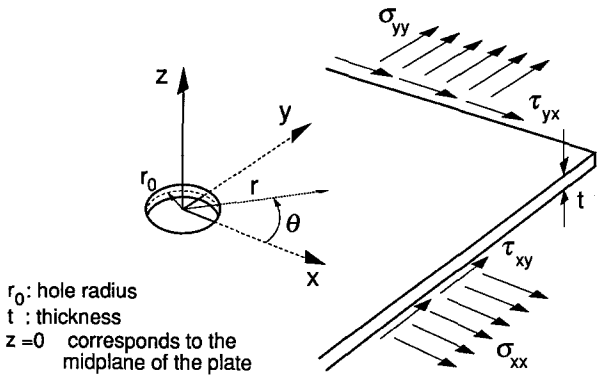

Fig. 1—Through hole in a thin plate subjected to uniform biaxial stresses

where

u_r, u_θ, u_z = cylindrical components of the displacement field
E = Young's modulus
ν = Poisson's ratio
ρ = ratio of hole radius to radial coordinate (r_0/r)
t = plate thickness

These equations can be conveniently written as

$$u_r = \tilde{A}(\sigma_{xx} + \sigma_{yy}) + \tilde{B}[(\sigma_{xx} - \sigma_{yy}) \cos 2\theta + 2\tau_{xy} \sin 2\theta]$$

$$u_\theta = \tilde{C}[(\sigma_{xx} - \sigma_{yy}) \sin 2\theta - 2\tau_{xy} \cos 2\theta]$$

$$u_z = \tilde{G}[(\sigma_{xx} - \sigma_{yy}) \cos 2\theta + 2\tau_{xy} \sin 2\theta] \quad (2)$$

where

$$\tilde{A} = \frac{r_0}{2E}(1 + \nu)\rho \qquad \tilde{C} = -\frac{r_0}{2E}[2(1 - \nu)\rho + (1 + \nu)\rho^2]$$

$$\tilde{B} = \frac{r_0}{2E}[4\rho - (1 + \nu)\rho^3] \qquad \tilde{G} = \frac{\nu t}{E}\rho^2 \quad (3)$$

Equations (3) assume a plane-stress state. The introduction of a blind hole in a previously stressed material produces a complex three-dimensional stress state which cannot be described by plane-stress assumptions, and for which no closed form solution is known.[16,17] This problem will be addressed later in the context of stress calculation formulas.

Holographic Method

Holographic interferometry provides the means to detect the incremental displacements produced by the introduction of either a blind or through hole in a material under stress. Only the basic equations and concepts needed to develop the method for computing stresses will be explained here. The reader is referred, for example, to Vest[18] for a more complete treatment of the subject.

If a hologram is made of the surface of a region containing residual stress, and a hole drilled into the region, when the hologram is exposed again or viewed under real-time conditions, the result is a pattern of alternating dark and light fringes like the one shown in Fig. 2. The reconstructed wavefront from the original image of the unperturbed material interferes with the wavefront coming from the material deformed by the introduction of the hole. The net effect is the production of interference fringes whenever the phase shift is an integer multiple of π. Each dark or light fringe represents contours of constant phase shifts. At a given point in the material, the relationship between the phase shift and displacement is given by

$$\phi = \bar{K} \cdot \bar{u} \quad (4)$$

where

ϕ = phase shift
$\bar{K}$ = sensitivity vector
$\bar{u}$ = displacement vector

The sensitivity vector is dependent on the illumination and viewing parameters of the experimental setup and is found as the vector difference of the respective propagation vectors.[18]

$$\bar{K} = \bar{k}_2 - \bar{k}_1 \quad (5)$$

The propagation vectors $\bar{k}_1$ and $\bar{k}_2$ define the direction of the illumination and viewing directions for a particular point in the x-y plane identified by (r, θ) in Fig. 3. Regardless of the observer's position, the magnitudes of $\bar{k}_1$ and $\bar{k}_2$ are defined as

$$|\bar{k}_1| = |\bar{k}_2| = \frac{2\pi}{\lambda} \quad (6)$$

where λ = wavelength of the illumination source. The

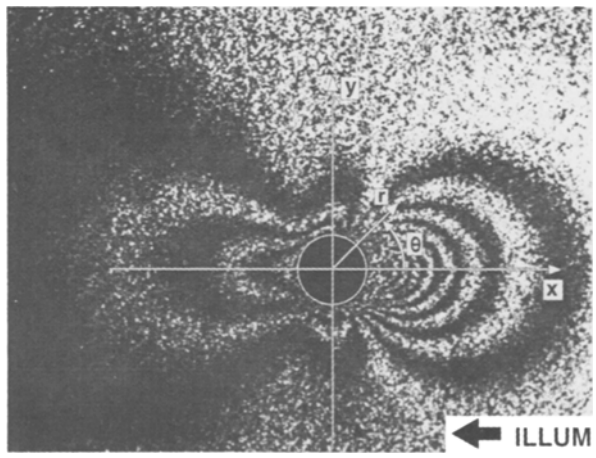

Fig. 2—Typical experimental fringe pattern for uniaxial stress

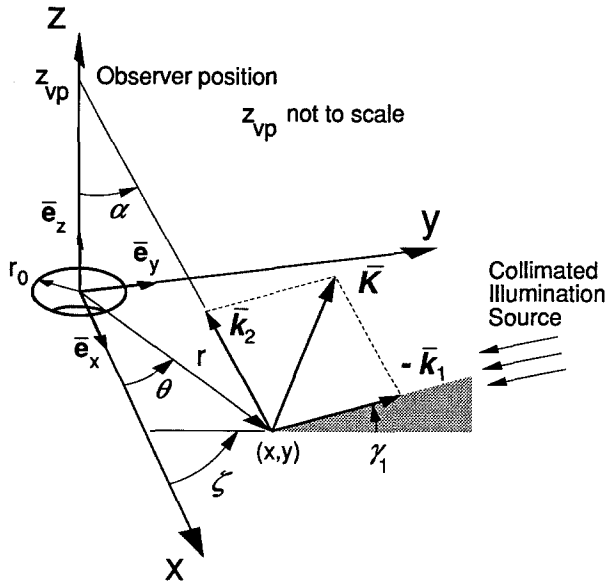

Fig. 3—Definition of propagation vectors and angles of illumination and viewing

illumination and viewing propagation vectors with the observer at finite distance z_{vp} from the hole, as indicated in Fig. 3, are then

$$\bar{k}_1 = -\frac{2\pi}{\lambda}[\cos\gamma_1 \cos\zeta\, \bar{e}_x + \cos\gamma_1 \sin\zeta\, \bar{e}_y + \sin\gamma_1\, \bar{e}_z]$$

$$\bar{k}_2 = \frac{2\pi}{\lambda}[-\sin\alpha\cos\theta\, \bar{e}_x - \sin\alpha\sin\theta\, \bar{e}_y + \cos\alpha\, \bar{e}_z] \quad (7)$$

where

γ_1 = grazing angle of the illumination source
ζ = inclination of the illumination direction with respect to the x axis
$\bar{e}_x, \bar{e}_y, \bar{e}_z$ = unit vectors along the x, y, and z axes of Fig. 3

and

$$\alpha = \tan^{-1}[(x^2 + y^2)^{1/2}/z_{vp}] = \tan^{-1}[r/z_{vp}] \quad (8)$$

z_{vp} = position of an observer along the z axis

The direction of the illumination propagation vector, which can have any orientation in space, has been defined by two angles, namely the grazing angle γ_1, which is measured in a plane normal to the x-y plane (Fig. 3), and the inclination with respect to the x axis, ζ, which is measured in the x-y plane. Alternative formulas to eq (8) can be derived for $\bar{k}_2$ if the viewer is not located along the z axis. The sensitivity vector is expressed as

$$\bar{K} = \frac{2\pi}{\lambda}[(\cos\gamma_1\cos\zeta - \sin\alpha\cos\theta)\bar{e}_x + (\cos\gamma_1\sin\zeta - \sin\alpha\sin\theta)\bar{e}_y + (\sin\gamma_1 + \cos\alpha)\,\bar{e}_z] \quad (9)$$

If the observer is at $z_{vp} \to \infty$, $\alpha = 0$ in Fig. 3 and the sensitivity vector is then

$$\bar{K}^0 = \frac{2\pi}{\lambda}[(\cos\gamma_1\cos\zeta)\bar{e}_x + (\cos\gamma_1\sin\zeta)\bar{e}_y + (1 + \sin\gamma_1)\bar{e}_z] \quad (10)$$

Equation (4) can now be expressed as

$$\phi = n\pi = K_x u_x + K_y u_y + K_z u_z \quad (11)$$

where

n = fringe order
u_x, u_y, u_z = Cartesian components of the displacement vector
K_x, K_y, K_z = Cartesian components of the sensitivity vector

In this expression, the phase shift is expressed as an integer multiple of π. With this notation, dark fringes are produced for $n = \pm 1, 3, 5, \ldots$ and light fringes for $n = \pm 0, 2, 4, \ldots$ Fractional fringe orders can be defined in the same form.

Equation (11) is fundamental to the interpretation of a given fringe pattern since it gives the relationship between the phase shifts, which can be extracted from the holographic interferogram in the form of fringe orders, and the unknown displacement field. Noting that the displacement field is in turn given by eqs (2) and the sensitivity vector is known from the illumination parameters, eq (11) will ultimately provide the means to compute the unknown components σ_{xx}, σ_{yy}, and τ_{xy} of the stress tensor.

Fringe-counting Method

A convenient method is needed for extracting the information from a given fringe pattern in order to evaluate the left-hand side of eq (11). One such method will now be described.

Equation 4 and hence eq (11) express the fact that a fringe pattern is sensitive only to the projection of the displacement vector $\bar{u}$ over the sensitivity vector, $\bar{K}$. With single beam illumination and for virtually all orientations of the sensitivity vector, both in-plane and out-of-plane components of the displacements intervene in the formation of the fringe pattern. This has the effect of producing a nonsymmetric fringe pattern, as seen in Fig. 2.

Although there is no requirement to work only with the in-plane components of hole-drilling displacements, the equations for computing stresses are simplified without the out-of-plane components. The influence of out-of-plane displacements in a fringe pattern

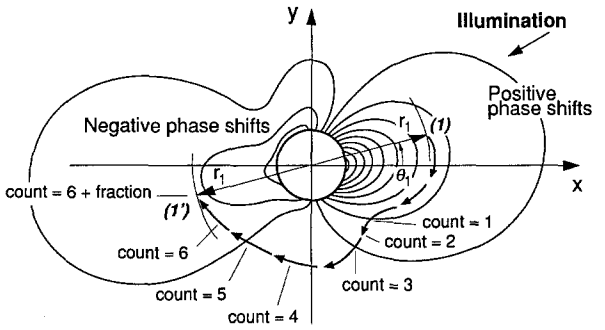

Fig. 4—Typical fringe counting path

can be circumvented using a straightforward fringe-counting method first applied in Ref. 10.

Suppose that a fringe pattern has the signs of its phase shifts known, as in Fig. 4. A fringe count is taken between two diametrically opposite points. For example, after picking a starting point centered on a light fringe located on the positive phase shift side, say point (1) identified by the radius r_1 and angle θ_1 with respect to the arbitrary set of x-y axes in Fig. 4, the fringe count is taken while 'hiking' to the diametrically opposite point (1′) on the negative phase shift side. The 'hiking' path can be the one indicated by arrows in Fig. 4 but other paths can be used as well. Each time a dark or light fringe is crossed, a positive or negative count of one is registered, taking care not to cross the same fringe twice to avoid 'double counting' . The sign of the count will depend on the direction of the 'hike'. This can be illustrated with the aid of Fig. 5. If the displacement field around the blind hole is known, for example through a finite-element analysis, eq (11) represents a three-dimensional surface defined in the x-y or r-θ plane when put in the form

$$\phi(r, \theta) = K_x(r, \theta)\, u_x(r, \theta) + K_y(r, \theta)\, u_y(r, \theta) + K_z(r, \theta)\, u_z(r, \theta) \qquad (r > r_0) \qquad (12)$$

This surface will be referred to as fringe function since it gives the value of the phase shift for all points of the domain around the hole.[19] Positive phase shifts will produce protruding regions whereas negative phase shifts will produce depressions. The fringe pattern can then be obtained by cutting this surface with planes of constant phase shifts in the same way topographical maps are made by cutting geographical features with constant elevation planes. The hiking path can be pictured over the three-dimensional fringe function surface as indicated in Fig. 5. A hike can either maintain constant 'elevation' or change it by crossing fringes. The hiking path shown in Figs. 4 and 5 requires changing elevation and thus crossing fringes. In this case the hike is downhill, starting from the positive phase shift side, and the fringe count increment is taken as positive each time a fringe is crossed. If the hike is uphill on the fringe function surface starting from the negative phase shift side, the fringe-count increment is negative. The experimental method used to determine phase shift signs in different regions will be described shortly.

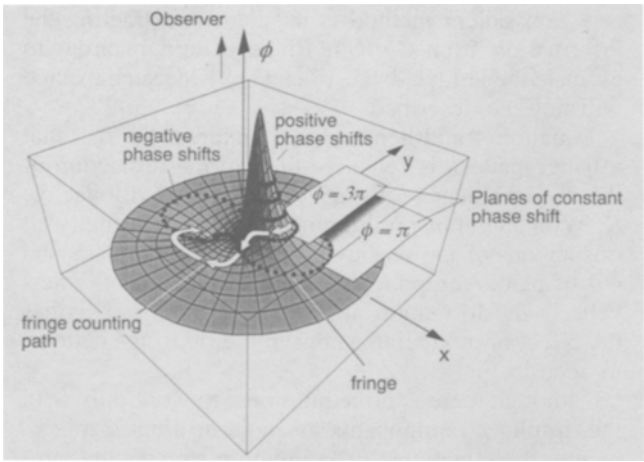

Fig. 5—Fringe function, fringe pattern, and a fringe counting path

Fractional fringe counts are possible since the ending point cannot coincide always with the center of a fringe. The final fringe count divided by two represents the fringe order of point (1) in Fig. 4 if there are no out-of-plane displacements, as will be shown. This fringe-counting method relies on relative fringe orders without the advance knowledge of absolute fringe orders but ultimately ends up finding an absolute fringe count whether or not the zero order fringe is crossed somewhere during the counting process. As a side effect, this fringe-counting procedure assures cancellation of out-of-plane displacement effects as will also be shown. A special case occurs when starting and ending a fringe count on the zero order fringe or on the same fringe; in such cases the fringe count is taken as zero.

If under a given residual stress state a hypothetical hologram were somehow to capture a fringe pattern insensitive to out-of-plane displacements, its positive and negative phase shift lobes would be perfectly symmetric. In such a case, the fringe orders at diametrically opposite points inside the lobes would have the same value, n^0, differing only in their sign. The actual fringe pattern that includes the effects of out-of-plane displacements for the same residual-stress state and illumination conditions is nonsymmetric, as in Figs. 2 and 4. Therefore, fringe orders at the homologous diametrically opposite points are, in general, not only of opposite sign but of different value. If the fringe order at point (1) of Fig. 4 is $n^{(1)}$ and is $n^{(1')}$ at the diametrically opposite point (1′), the fringe-counting method outlined previously asserts that

$$\frac{n^{(1)} - n^{(1')}}{2} = n^0 \qquad (13)$$

The operation indicated above is actually the average of a relative fringe count and its validity is maintained even in cases where the starting and ending points of a hike, (1) and (1′), are in a region where the phase shift sign remains the same over the path of the hike.

This interpretation generalizes the sign assignment for fringe counts. Downhill hikes always produce positive counts while uphill hikes produce negative counts. Regardless of the phase shift signs of the starting and ending points, downhill hikes produce a positive n^0, since $n^{(1)} > n^{(1')}$. The opposite is true for uphill hikes.

Taking into account the relations between cylindrical and Cartesian components of displacements and eqs (11) and (12), the fringe orders $n^{(1)}$ and $n^{(1')}$ can be expressed as

$$\begin{aligned}\pi n^{(1)} &= (K_x^{(1)} \cos\theta_1 + K_y^{(1)} \sin\theta_1)\, u_r(r_1, \theta_1) \\ &\quad + (-K_x^{(1)} \sin\theta_1 + K_y^{(1)} \cos\theta_1)\, u_\theta(r_1, \theta_1) \\ &\quad + K_z^{(1)}\, u_z(r_1, \theta_1) \\ \pi n^{(1')} &= -[K_x^{(1')} \cos\theta_1 + K_y^{(1')} \sin\theta_1]\, u_r(r_1, \theta_1 + \pi) \\ &\quad -[-K_x^{(1')} \sin\theta_1 + K_y^{(1')} \cos\theta_1]\, u_\theta(r_1, \theta_1 + \pi) \\ &\quad + K_z^{(1')}\, u_z(r_1, \theta_1 + \pi) \qquad (14)\end{aligned}$$

where $K_i^{(1)}$, $K_i^{(1')}$ = Cartesian components of the sensitivity vector at points (1) and (1′) in Fig. 4. In these expressions, the displacements at diametrically opposite points have the same value and sign since according to eqs (2) they depend on *cos 2θ* and *sin 2θ*.

Substituting the expressions for the components of the sensitivity vectors from eq (9) and subtracting eqs (14) to form an average fringe order,

$$\begin{aligned}\pi \frac{n^{(1)} - n^{(1')}}{2} &= \frac{2\pi}{\lambda} \{[\cos\gamma_1 \cos\zeta \cos\theta_1 \\ &\quad + \cos\gamma_1 \sin\zeta \sin\theta_1]\, u_r(r_1, \theta_1) \\ &\quad + [-\cos\gamma_1 \cos\zeta \sin\theta_1 \\ &\quad + \cos\gamma_1 \sin\zeta \cos\theta_1]\, u_\theta(r_1, \theta_1)\} \qquad (15)\end{aligned}$$

The out-of-plane displacement component, u_z, dropped out in this last step. If the observer is sufficiently far from the object, such that angle α in Fig. 3 approaches zero, as is usually the case, then the following components of the sensitivity vector can be recognized from eq (10),

$$\begin{aligned}K_x^0 &= \frac{2\pi}{\lambda} \cos\gamma_1 \cos\zeta \\ K_y^0 &= \frac{2\pi}{\lambda} \cos\gamma_1 \sin\zeta \qquad (16)\end{aligned}$$

Using eqs (14) and (16), eq (15) becomes

$$\pi \frac{n^{(1)} - n^{(1')}}{2} = K_x^0 u_x + K_y^0 u_y = \pi n^0 \qquad (17)$$

This shows that the average fringe count performed between diametrically opposite points on a fringe pattern according to the procedure described before, gives an absolute fringe order, n^0, which excludes the influence of out-of-plane displacements. It is noted that knowledge of the absolute fringe orders, $n^{(1)}$ and $n^{(1')}$, is not required. Since the fringe counts are multiplied by π, eq (17) actually expresses a relationship between phase shifts and displacements. The fringe count may also be viewed as representing the in-plane component of displacement parallel to the direction of illumination.[20]

Stresses

Equation 17 provides the starting point for obtaining stresses from the fringe-counting procedure. A direct relationship between the unknown components of the stress tensor and the fringe count can be obtained by substituting eqs (2) into eq (17) using the relations between cylindrical and Cartesian components of displacements,

$$\begin{aligned}\pi n^0 &= (K_x^0 \cos\theta + K_y^0 \sin\theta)\, \{\tilde{A}(\sigma_{xx} + \sigma_{yy}) \\ &\quad + \tilde{B}[(\sigma_{xx} - \sigma_{yy}) \cos 2\theta + 2\tau_{xy} \sin 2\theta]\} \\ &\quad + (-K_x^0 \sin\theta + K_y^0 \cos\theta)\{\tilde{C}[(\sigma_{xx} \\ &\quad - \sigma_{yy}) \sin 2\theta - 2\tau_{xy} \cos 2\theta]\}\end{aligned}$$

After rearranging,

$$\begin{aligned}\pi n^0 &= \{(K_x^0 \cos\theta + K_y^0 \sin\theta)(\tilde{A} + \tilde{B} \cos 2\theta) \\ &\quad + (-K_x^0 \sin\theta + K_y^0 \cos\theta)\, \tilde{C} \sin 2\theta\}\sigma_{xx} \\ &\quad + \{(K_x^0 \cos\theta + K_y^0 \sin\theta)(\tilde{A} - \tilde{B} \cos 2\theta) \\ &\quad - (-K_x^0 \sin\theta + K_y^0 \cos\theta)\, \tilde{C} \sin 2\theta\}\sigma_{yy} \\ &\quad + 2\{(K_x^0 \cos\theta + K_y^0 \sin\theta)(\tilde{B} \sin 2\theta) \\ &\quad - (-K_x^0 \sin\theta + K_y^0 \cos\theta)\, \tilde{C} \cos 2\theta\}\tau_{xy} \qquad (18)\end{aligned}$$

When the fringe count is performed for three different pairs of diametrically opposite points around a hole, eq (18) originates a system of linear equations which can be put in matrix form as

$$\pi \begin{Bmatrix} n_1^0 \\ n_2^0 \\ n_3^0 \end{Bmatrix} = \begin{bmatrix} C_{11} & C_{12} & C_{13} \\ C_{21} & C_{22} & C_{23} \\ C_{31} & C_{32} & C_{33} \end{bmatrix} \begin{Bmatrix} \sigma_{xx} \\ \sigma_{yy} \\ \tau_{xy} \end{Bmatrix} \qquad (19)$$

where the ith fringe count is found as

$$n_i^0 = \frac{n_i^{(i)} - n_i^{(i')}}{2}$$

Assuming all fringe counts are taken at the same radius, but at different angles θ_i with respect to the arbitrary set of axis of Fig. 4, the coefficients C_{ij} of eq (19) can be expressed as

$$C_{i1} = (K_x^0 \cos\theta_i + K_y^0 \sin\theta_i)(\tilde{A} + \tilde{B}\cos 2\theta_i) + (-K_x^0 \sin\theta_i + K_y^0 \cos\theta_i)\tilde{C} \sin 2\theta_i$$

$$C_{i2} = (K_x^0 \cos\theta_i + K_y^0 \sin\theta_i)(\tilde{A} - \tilde{B}\cos 2\theta_i) - (-K_x^0 \sin\theta_i + K_y^0 \cos\theta_i)\tilde{C} \sin 2\theta_i$$

$$C_{i3} = 2\{(K_x^0 \cos\theta_i + K_y^0 \sin\theta_i)(\tilde{B} \sin 2\theta_i) - (-K_x^0 \sin\theta_i + K_y^0 \cos\theta_i)\tilde{C} \cos 2\theta_i\} \quad (20)$$

The unknown components of the stress tensor can then be found by inverting eq (19).

$$\begin{Bmatrix} \sigma_{xx} \\ \sigma_{yy} \\ \tau_{xy} \end{Bmatrix} = \pi \begin{bmatrix} C_{11} & C_{12} & C_{13} \\ C_{21} & C_{22} & C_{23} \\ C_{31} & C_{32} & C_{33} \end{bmatrix}^{-1} \begin{Bmatrix} n_1^0 \\ n_2^0 \\ n_3^0 \end{Bmatrix} \quad (21)$$

The principal stresses, σ_1 and σ_2, and their directions can then be found using the following expressions.

$$\sigma_1, \sigma_2 = \frac{\sigma_{xx} + \sigma_{yy}}{2} + \sqrt{\left(\frac{\sigma_{xx} - \sigma_{yy}}{2}\right)^2 + \tau_{xy}^2} \quad (22)$$

$$\beta = 45 \text{ deg } (1 - \text{sign } [\sigma_{xx} - \sigma_{yy}]) \cdot (1 - \delta(\sigma_{xx} - \sigma_{yy})) + \frac{1}{2}\tan^{-1}\left(\frac{2\tau_{xy}}{\sigma_{xx} - \sigma_{yy}}\right)$$

where

β = angle between the illumination direction and σ_1

$\delta(\ )$ = impulse function

sign [ ] = sign function

$$\text{sign } [x] = \begin{cases} +1 \text{ if } x > 0 \\ -1 \text{ if } x < 0 \end{cases} \qquad \delta(x) = \begin{cases} 0 \text{ if } x \neq 0 \\ 1 \text{ if } x = 0 \end{cases}$$

Two items, which are addressed in the next sections, remain unsolved on the right-hand side of eq (21). The first involves determination of signs of phase shifts in different regions of the fringe pattern, and the second an expression for the coefficients $\tilde{A}$, $\tilde{B}$, and $\tilde{C}$ in eqs (20). It is noted that knowledge of the phase shift signs of the starting and ending points allows the experimenter to detect if a hike goes uphill or downhill during a fringe count, and thus defines the signs of n_1^0, n_2^0, and n_3^0.

Determination of Fringe Orders and Phase-shift Signs

Phase-shift signs are in general associated with the direction of the displacements captured by a holographic fringe pattern. Determination of absolute fringe orders and phase-shift signs in a given holographic fringe pattern is an issue addressed by several authors who offer solutions that, although original in nature, cannot be easily applied when measuring residual stresses by the hole-drilling method. Ennos[21] correctly pointed out that a static fringe pattern fails to identify the sign of the phase shift of a given fringe and proposed its deduction from a 'live fringe' experiment. Jones and Wykes[22] describe in detail the identification of fringe orders and their signs by observing the motion of fringes using real-time holography while incremental loads are applied to the object under study. Unfortunately, this dynamic method is not applicable for measuring residual stresses since the experimenter cannot control the loading source, i.e., the residual stresses. Hariharan and Ramprasad[23] demonstrate the introduction of 'background' fringes by manipulating various optical parameters in order to eliminate the ambiguity in the phase-shift sign. Related approaches utilizing 'carrier fringes' have been applied by Plotkowski *et al.*,[24] Matthys *et al.*[25] and Guo *et al.*[26] Ostrovsky *et al.*[17] maintain the displacement sign and therefore the phase-shift sign cannot be determined from a fringe pattern when measuring residual stresses using an optical setup sensitive only to out-of-plane displacements.

As it turns out, phase-shift signs can indeed be extracted from a fringe pattern without the need for extra equipment or resorting to incremental loading. Reference 10 describes a simple dynamic method based on the perturbation of the reference beam in a real-time holographic setup after a hole is drilled and a fringe pattern is visible. The perturbation can be easily introduced by a momentary shortening of the optical path in the reference beam, for example by gently pushing a mirror located in its path. The response of the fringe pattern to such a perturbation is a change in configuration or continuous 'flow' of fringes to adjacent positions as indicated in Fig. 6. Fringe lobes can be classified according to their shrinking or expanding behavior. Regions with shrinking fringes undergo displacements towards the illumination source and are assigned a positive phase shift sign. If the phase shift ϕ is positive, then according to eq (4),

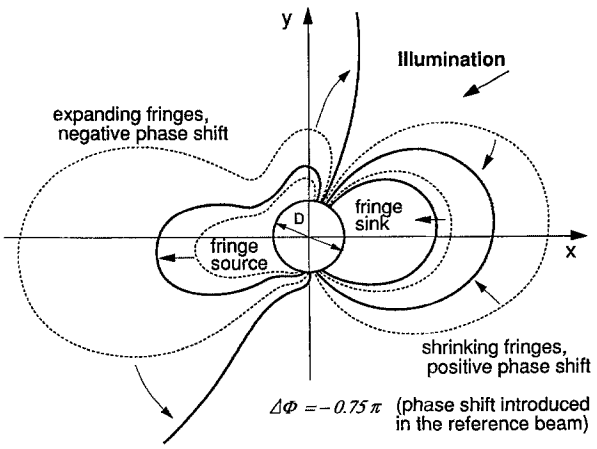

Fig. 6—Fringe pattern flow under reference-beam path perturbation (shortening)

$\boldsymbol{K} \cdot \boldsymbol{u} > 0$, indicating that the displacement vector forms an acute angle with the sensitivity vector. The fringe pattern registers the component of the displacements directed towards the illumination source. Regions with expanding fringes experience displacements away from the illumination source and are assigned negative phase shift signs.

The reason for this behavior becomes clear when the phenomenon is explained with the aid of the fringe function described by eq (12). A shortening of the reference beam path is equivalent to the introduction of an extra negative phase shift term in eq (12), as can be shown from analysis of the irradiance distribution of a holographic plate. Therefore, the fringe function can now be expressed as

$$\phi(r, \theta) = K_x(r, \theta)\, u_x(r, \theta) + K_y(r, \theta)\, u_y(r, \theta) + K_z(r, \theta)\, u_z(r, \theta) + \Delta\Phi \qquad (23)$$

where $\Delta\Phi = \Phi_R < 0$ = net phase shift introduced by reference beam path shortening.

The surface representing the original fringe function can be pictured as 'sinking' an amount $\Delta\Phi$ with respect to its original position while maintaining its overall shape. An intuitive explanation of the corresponding effects on a fringe pattern considers a series of planes fixed in space, each representing a given phase-shift value. When the fringe function surface sinks, these planes will continuously cut different sections of the surface giving a succession of fringe patterns. The resulting effect will give the observer the impression of viewing shrinking fringes in those regions where the fringe function exhibits protrusions, i.e., positive phase shifts, and expanding fringes where the fringe function exhibits depressions, i.e., negative phase shifts.

Figure 7 shows the sunken surface of the fringe function with the current fringes after a phase shift $\Delta\Phi = -0.75\pi$ has been introduced in the reference beam path. Two planes of constant phase shift are drawn with the cutout profiles of the fringes before the surface downward movement showing the fringe shrinkage effect for positive phase shift regions. The gap between current and former fringe positions represent the successive positions of the fringe if the downward movement is continuous. It is noted that the current and former fringe positions are at the same level.

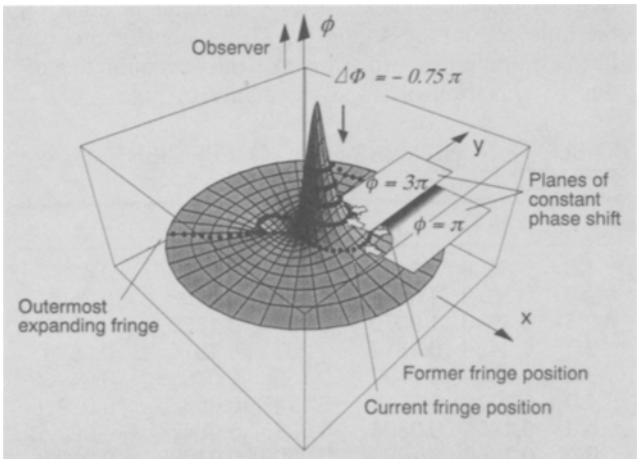

Fig. 7—Visualization of fringe flow under reference-beam perturbation with the aid of the fringe function

An interesting situation develops in the transition region between protrusions and depressions in the fringe function when $|\Delta\Phi| > \pi$. The outermost expanding fringe crosses the location of the original zero order fringe and enters the protruding region giving the impression of snapping into a shrinking fringe. In other words, expanding fringe regions act as fringe sources whereas shrinking fringe regions act as fringe sinks.

If the object beam optical path is shortened instead, the effects are opposite to those discussed above. Expanding fringes now indicate regions with positive phase shifts and shrinking fringes regions with negative phase shifts. This is due to the sign of the resulting phase shift, $\Delta\Phi = \Phi_0 > 0$. Now the fringe function surface 'rises' an amount $\Delta\Phi$ with respect to its original position.

An example of the determination of signs of phase shifts for an actual fringe pattern will be given shortly.

Correction of the Plane-stress Displacement Formulas

The displacement formulas, eqs (2), and therefore the stress calculation formulas, eqs (20)–(21), with coefficients defined by eq (3) are only applicable when plane-stress assumptions are valid. As pointed out earlier, a blind hole produces a complex three-dimensional stress state in its surrounding area which cannot be described by plane-stress solutions. However, following Schajer,[27] the displacements still have the general form expressed by eqs (2) but with a different set of coefficients $\tilde{A}$ through $\tilde{G}$. These coefficients can be determined from the displacement data of a finite-element modeling of the blind-hole drilling process.

If a blind hole is drilled in a material subjected to a uniaxial uniform stress, σ_{xx}, the cylindrical components of the displacement field around the hole are assumed to be expressed by Fourier expansions of the type[16]

$$u_r(r, \theta, z) = \sum_{n=0}^{\infty} u_{rn}(r, z) \cos n\theta$$

$$u_\theta(r, \theta, z) = \sum_{n=0}^{\infty} u_{\theta n}(r, z) \sin n\theta$$

$$u_z(r, \theta, z) = \sum_{n=0}^{\infty} u_{zn}(r, z) \cos n\theta \qquad (24)$$

As a first approximation only the terms $n = 0$ and n

= 2 (not to be confused with fringe orders) are retained, giving the following expressions.

$$u_r(r, \theta) = (\tilde{A} + \tilde{B} \cos 2\theta)\, \sigma_{xx}$$

$$u_\theta(r, \theta) = (\tilde{D} + \tilde{C} \sin 2\theta)\, \sigma_{xx}$$

$$u_z(r, \theta) = (\tilde{F} + \tilde{G} \cos 2\theta)\, \sigma_{xx} \qquad (25)$$

$\tilde{A}$, $\tilde{B}$, $\tilde{C}$, $\tilde{F}$, and $\tilde{G}$ are coefficients yet to be determined. In general, these coefficients will depend on the elastic constants, the hole dimensions, the location given by the ratio $\rho = r_0/r$, and the hole depth to diameter ratio, h/D.

The meaning of eqs (25) can be explained with the aid of Fig. 8. For a constant radius, i.e., at a constant ratio ρ, the displacements vary as harmonic functions superposed on a constant. Therefore, the coefficients $\tilde{A}$ through $\tilde{G}$ for a given ratio ρ can be found from the displacements of a single finite-element run as follows:

$$\tilde{A} = \frac{u_r|_{\theta=45\ \text{deg}}}{\sigma_{xx}} \qquad \tilde{B} = \frac{u_r|_{\theta=0\ \text{deg}} - u_r|_{\theta=45\ \text{deg}}}{\sigma_{xx}}$$

$$\tilde{C} = \frac{u_\theta|_{\theta=45\ \text{deg}}}{\sigma_{xx}} \qquad \tilde{D} = \frac{u_\theta|_{\theta=0\ \text{deg}}}{\sigma_{xx}} = 0$$

$$\tilde{F} = \frac{u_z|_{\theta=45\ \text{deg}}}{\sigma_{xx}} \qquad \tilde{G} = \frac{u_z|_{\theta=0\ \text{deg}} - u_z|_{\theta=45\ \text{deg}}}{\sigma_{xx}} \qquad (26)$$

where $u_r|_{\theta=45\ \text{deg}}$ = nodal displacement in the radial direction at $\theta = 45$ deg and $r = r_0/\rho$.

These formulas have been derived from eqs (25) by taking a pair of values for θ, 0 deg and 45 deg, at a given radial distance from the blind hole. Alternative formulas can be found for any other pair of values for θ. Although these coefficients are found from a finite-element model under uniaxial load, they are also valid for the biaxial displacement formulas, eqs (2), provided the superposition principle holds. It is noted that these coefficients are independent of the stress level and are only valid for a particular ratio ρ, a given hole depth to diameter ratio h/D, a given hole diameter, and a given set of elastic constants.

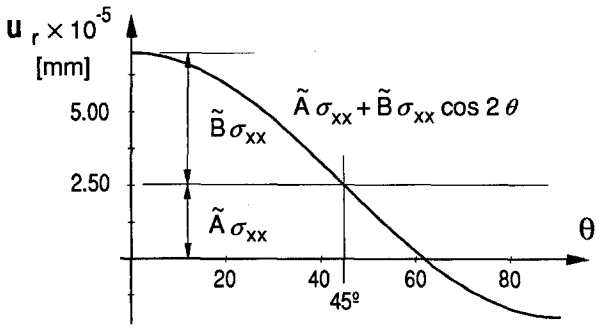

Fig. 8—Circumferential variation of radial displacements at a constant radius around a hole

In order to make the coefficients independent of hole diameter and possibly the elastic constants, it is convenient to define the following nondimensional coefficients,

$$\tilde{a} = \frac{2E}{r_0(1+\nu)}\tilde{A} \qquad \tilde{b} = \frac{2E}{r_0}\tilde{B} \qquad \tilde{c} = \frac{2E}{r_0}\tilde{C}$$

$$\tilde{f} = \frac{2E}{r_0}\tilde{F} \qquad \tilde{g} = \frac{2E}{4\nu r_0}\tilde{G} \qquad (27)$$

The choice for the normalizing parameters was guided by the form of the coefficients in the original plane-stress formulas, eqs (3). Note that the hole radius is used above to make the $\tilde{f}$ and $\tilde{g}$ coefficients nondimensional instead of half the material thickness ($t/2$) as in the plane-stress formulas.

The coefficients $\tilde{A}$ through $\tilde{G}$ as computed by finite-element analysis are dependent on Poisson's ratio to varying degrees. However, it was found that the nondimensional coefficients $\tilde{a}$ and $\tilde{b}$ had little or no dependence on Poisson's ratio, the dependence of $\tilde{f}$ is weak, while for $\tilde{c}$ and $\tilde{g}$ it can be significant. Values of $\tilde{f}$ and $\tilde{g}$ are not needed for stress calculations when the fringe-counting method is employed since those coefficients pertain to out-of-plane deformations which are cancelled out by the method. Even though $\tilde{c}$ exhibits dependence on Poisson's ratio, the resulting influence on stress calculations is minimal as discussed later.

Table 1 shows the nondimensional coefficients obtained from finite-element modeling of a 1.58-mm (0.062-in.) diameter blind-hole drilling process in a material with $\nu = 0.3$ and stressed uniaxially at 186 MPa (27 ksi). The values are listed according to the radial locations expressed by multiples of the hole radius, r_0. Even though these values have been obtained using a model with a specific residual-stress level and hole diameter, they can be used for other stress levels and hole diameters by virtue of eqs (26) and (27).

Values for Table 1 have been obtained considering a full hole depth, h, of 1.2 times the blind hole diameter, D, and a hole drilled into a plate where the ratio of plate thickness to hole diameter is eight. If the hole depth is less than 1.2 D, the coefficients can be recomputed in order to take into account the reduced relaxation of stress by shallower holes.

TABLE 1—NONDIMENSIONAL COEFFICIENTS FROM FINITE-ELEMENT ANALYSIS

r/r_0	$\tilde{a}$	$\tilde{b}$	$\tilde{c}$	$\tilde{f}$	$\tilde{g}$
1.5	0.6808	1.8626	−0.7514	0.2763	0.4257
2.0	0.5073	1.4170	−0.4206	0.2098	0.2595
2.5	0.3943	1.0870	−0.2814	0.1530	0.1529
3.0	0.3136	0.8517	−0.2071	0.1074	0.0879
3.5	0.2534	0.6792	−0.1630	0.07555	0.04752
4.0	0.2073	0.5512	−0.1347	0.05325	0.02216
5.0	0.1456	0.3854	−0.0995	0.02474	−0.00270
6.0	0.1069	0.2865	−0.0805	0.01033	−0.01206

Note: valid only for hole depth to diameter ratio, h/D = 1.2

Summarizing, all nondimensional coefficients are independent of the hole radius and Young's modulus. They are still dependent on the particular ratio ρ, a given hole depth to diameter ratio (h/D), and Poisson's ratio in the case of $\tilde{c}$ and $\tilde{g}$. Once the fringe count is performed at a given radial location around a hole, stress calculations can proceed using eqs (21)–(22) with coefficients $\tilde{A}$, $\tilde{B}$, and $\tilde{C}$ obtained from Table 1 and eqs (27).

The finite-element mesh used for obtaining all of the data in Table 1 is shown in Fig. 9. Due to the symmetry of the problem, only a quarter of a 27.94 × 27.94 × 12.7-mm (1.1 × 1.1 × 0.5-in.) square plate was considered with the appropriate boundary conditions. The model was built with 4725 three-dimensional eight- and six-node constant-strain isoparametric elements using the Abaqus code. The blind-hole drilling process was simulated by inactivating elements representing removed material after the model had been loaded to the desired stress level. When incremental drilling is required, the elements have to be inactivated in several steps after the initial loading. The model is considered to be subjected to uniaxial stress in the x direction.

The displacement data obtained from the finite-element analysis can also be processed in order to produce synthetic fringe patterns by solving eq (12) for integer values of n at discrete points around the hole. The result is a series of points defined by their coordinates, either (x, y) or (r, θ), which can be plotted using a desktop computer. The fringe pattern shown in Fig. 4 was obtained using this method.

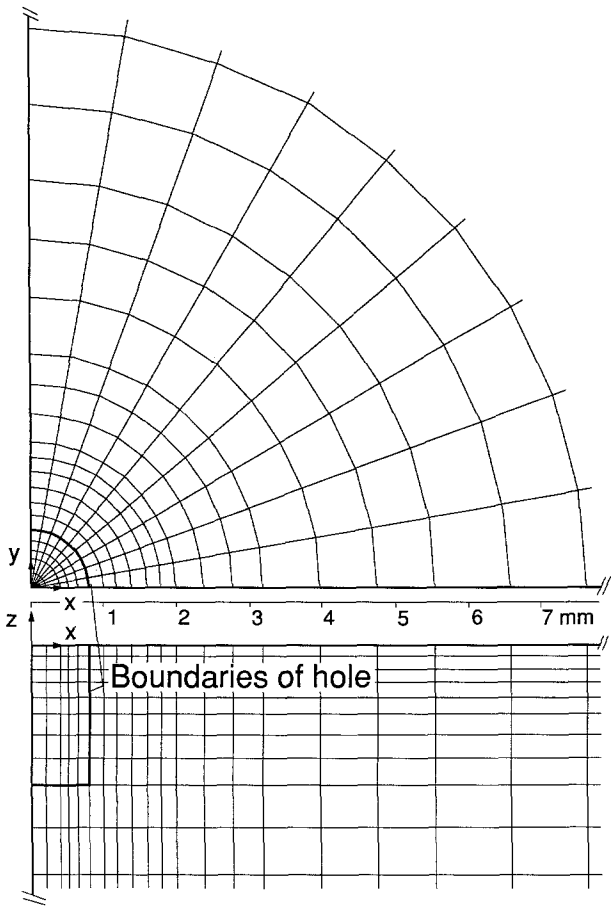

Fig. 9—Finite-element mesh

Illustrative Example

In order to generate fringe patterns to check the ability of the holographic/hole-drilling technique to determine residual stresses, a series of experiments were conducted using specimens with known stresses. The details of the experiments are described in Refs. 14 and 28. The results of one of the experiments will be considered here for the purpose of illustrating application of the theoretical approach derived in this paper. A more comprehensive comparison of stresses determined by the holographic technique with those determined from other methods is also provided in Ref. 14.

The experiment to be considered here utilized an interference fit between two thick-walled hollow cylinders to produce a uniaxial circumferential residual stress. The cylinders were made of stress-relieved aluminum alloy 7075-T651. The circumferential stresses were calculated from theory and estimated from conventional strain-rosette hole-drilling measurements to be between 186 and 200 MPa (27 and 29 ksi). Figure 10 shows the interference fringe pattern obtained when the illumination axis was at 30 deg to the circumferential stress direction. Relevant test parameters are given in Table 2. An arbitrary set of axes with an origin at the center of the hole has been taken with the x direction coincident with the illumination direction. This particular choice simplifies the expression for the sensitivity vector since ζ = 0 deg in eqs (9) and (10). However, any other coordinate axes orientation could be used without loss of generality.

The starting points for the fringe-counting procedure are labeled as (1), (2), and (3), the ending points as (1′), (2′), and (3′). They are all located at the same

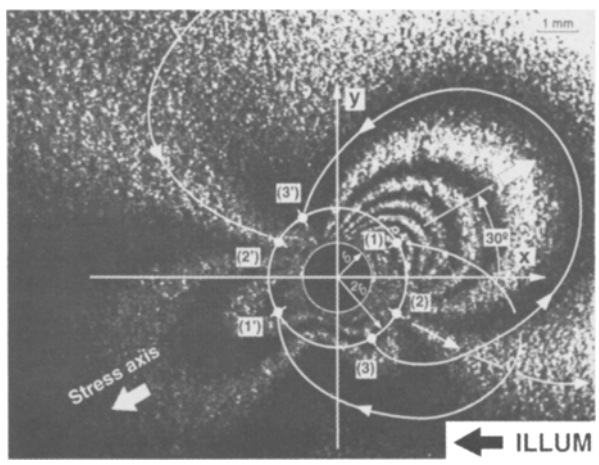

Fig. 10—Fringe pattern with the illumination direction at 30 deg to direction of uniaxial stress

TABLE 2—DATA FOR CALCULATING STRESSES FROM THE FRINGE PATTERN OF FIG. 10

Young's modulus	E = 71.0 GPa (10.3 × 10^6 psi)
Poisson's ratio	ν = 0.33
Grazing angle	γ_1 = 23.5 deg
Illumination direction	ζ = 0 deg
Illumination wavelength	λ = 514.5 × 10^{-9} m
Hole diameter	D = 1.68 mm (0.066 in.)
Hole depth	h = 2.03 mm (0.08 in.)
Fringe count radial location	$r = D$ = 1.68 mm
Angles and fringe counts	θ_1 = 30 deg, n_1^0 = 7.7
	θ_2 = −31 deg, n_2^0 = 0
	θ_3 = −60 deg, n_3^0 = −2

radial distance, $r = 2r_0$, from the center of the hole. Other radial locations could have been used as well.

The inclination with respect to the x axis of the segment joining (1) and (1′) is θ_1 = 30 deg. The inclinations of the segments (2)–(2′) and (3)–(3′) are θ_2 = −31 deg and θ_3 = −60 deg respectively. The strategy followed for these choices was to maximize the fringe counts for the points (1)–(1′) and (3)–(3′). The points (2)–(2′) were chosen to make the fringe count zero in order to remove any fractional fringe estimation errors. As a practical note, this situation may not be present in all fringe patterns. It should be also noted that other starting and ending points could have been used as well.

The hiking paths and directions for the fringe counts are indicated with white lines and arrows. The starting point (1) is centered on a dark fringe in a region of shrinking fringes if the reference beam path length is shortened. The hike ends on the edge of another dark fringe which expands when the reference beam path is shortened. The hike is downhill and the counting increments are thus positive. The count divided by two is estimated to be 7.7. Starting point (2) is centered on a bright fringe located between shrinking and expanding fringes which suggests that it is the zero-order fringe. After circling outside the zone seen in Fig. 10, the hike ends on the same fringe giving a zero count. Starting point (3) is located in a region of expanding fringes which indicates negative counting increments. The final fringe count divided by two is −2.

Using the information summarized in Table 2, and the stress calculation formulas, eqs (21)–(22), with coefficients $\tilde{A}$, $\tilde{B}$, and $\tilde{C}$ defined by the plane stress formulas, eqs (3), the following values of principal stresses and directions are found:

$$\sigma_1 = 194 \text{ MPa (28.1 ksi)}$$

$$\sigma_2 = 32 \text{ MPa (4.7 ksi)}$$

$$\beta = 36 \text{ deg}$$

If the coefficients $\tilde{A}$, $\tilde{B}$, and $\tilde{C}$ are derived instead from the finite-element-based nondimensional coefficients of Table 1, the principal stresses and directions for the same experimental data are computed to be

$$\sigma_1 = 194.4 \text{ MPa (28.2 ksi)}$$

$$\sigma_2 = -22 \text{ MPa (−3.2 ksi)}$$

$$\beta = 30 \text{ deg}$$

The differences between stresses determined by plane-stress and finite-element formulations are indeed small in this case, and both sets of values agree well with the level of residual stress in the interference fit specimen. However, if fringe counts are taken at greater distances from the center of the hole, discrepancies become noticeable. For example, Fig. 11 shows the differences when counts are taken as a function of r/r_0. The values for σ_1 obtained using the plane-stress solution tend to drop with respect to the finite-element formulation as counts are taken at increasing distance from the center of the hole for $r > 2r_0$. However, the values for σ_2 tend to maintain about the same difference between both solutions.

The above finite-element-based stress calculations were made considering Poisson's ratio as ν = 0.33, a typical value for aluminum, but without making any corrections to the nondimensional coefficients $\tilde{a}$, $\tilde{b}$, and $\tilde{c}$, of Table 1 which were calculated assuming ν = 0.3. When calculating coefficients, $\tilde{A}$, $\tilde{B}$, and $\tilde{C}$, the influence of Poisson's ratio appears implicitly in the nondimensional coefficients $\tilde{a}$, $\tilde{b}$, and $\tilde{c}$, and explicitly in the expression for $\tilde{A}$,

$$\tilde{A} = \frac{r_0(1+\nu)}{2E}\tilde{a}$$

Extensive computations have shown that use of the actual Poisson's ratio in this equation without correcting any of the nondimensional coefficients yields stress values very close to those obtained when corrections are made. In fact, it was found that the use of nondimensional coefficients in Table 1 for cases where Poisson's ratio varied between 0.25 and 0.35 caused computed stresses to differ by a few percent at most. For example, the values of $\tilde{a}$, $\tilde{b}$, and $\tilde{c}$ listed in Table 1 can be recomputed by running the finite-

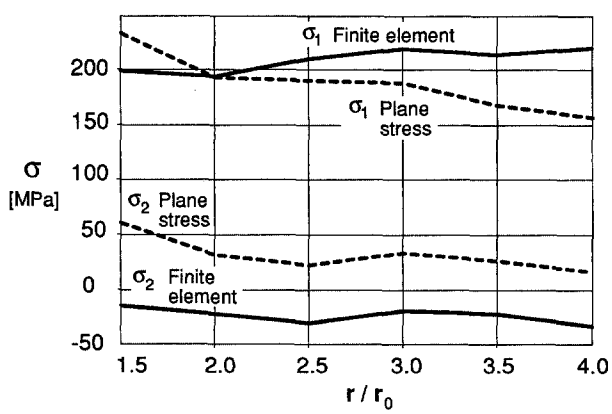

Fig. 11—Differences in stresses estimated by plane-stress and finite-element solutions

element model for $\nu = 0.33$. The stresses can be then recomputed for the data listed in Table 2 yielding the following values.

$$\sigma_1 = 193 \text{ MPa } (27.9 \text{ ksi})$$

$$\sigma_2 = -24 \text{ MPa } (-3.4 \text{ ksi})$$

$$\beta = 29 \text{ deg}$$

Discussion

Holographic interferometry used in conjunction with blind-hole drilling provides an accurate, fast technique for determining residual stresses while eliminating most of the drawbacks associated with the conventional strain-gage-rosette technique. However, the holographic technique does require rather strict vibration isolation during the exposure of the holographic plate, which is usually on the order of a second. Since vibration isolation is typically obtained by means of an optical table, the scale of the structures or components that can be mounted on it is limited by its size.

The holographic/hole-drilling technique should be applicable, as currently derived, for determining uniform components of stresses in the presence of stress gradients acting along a surface if the hole is sufficiently small relative to the dimensions over which the gradients exist and if the uniform components of stress are sufficiently large relative to the varying components of stress. The meaning of 'sufficiently' needs to be investigated as well as possible ways of extending the technique to determine surface stress gradients.

The holographic/hole-drilling technique could also be used to determine stress gradients below a surface by recording fringe patterns, viewed in real time, at various increments of hole depth and then processing the optical information as a function of depth in conjunction with displacement-based approaches similar to strain-based approaches such as given in Refs. 16 and 27.

The use of holes smaller than those considered here is certainly feasible. Experiments utilizing 0.8-mm (0.031-in.) diameter holes have been used successfully to determine stresses, as described in Ref. 14.

Perturbation of a fringe pattern need not be done by manually touching the back of a mirror in the reference or object beam paths. Instead, a known phase shift of any desired amount could be introduced by optical means, e.g., by interposition of a compensator in the object or reference beam paths. Thus, the 'flowing' effect of fringes can always be obtained either in a continuous or discrete fashion.

The extra phase shift term in eq (23), $\Delta\Phi$, can actually be regarded as time-dependent since the reference-beam path length varies with time until a limit is reached. The method of perturbing the fringe pattern by a time-dependent variation of the optical path length of the reference beam is hardly new, but to our knowledge it has not been applied before to deduce phase-shift signs in holographic interferometry by simple observation. The interpretation of fringe patterns as level curves of a three-dimensional surface has originally been reported by Holloway and Durelli[29] for an analysis of out-of-plane displacements originated by stress waves. In this paper, that interpretation has been extended to a more general case including out-of-plane and in-plane displacements, and recognizing the time-dependent movement of the entire fringe function surface to explain the causality between directions of 'flowing fringes' and phase-shift signs.

It is noted that the process of converting fringe counts to stresses is valid as long as a given fringe pattern is unique, that is, there are no other stress states that produce the same fringe pattern under consideration. It has been found that for a given fringe pattern, originated by a stress state defined by the tensor σ_{ij}, it is possible to obtain an identical fringe pattern by simply reversing the sign of the stress tensor, i.e., $-\sigma_{ij}$. Although the fringe patterns for both cases look the same under static conditions, i.e., regarding a fringe pattern as a frozen two-dimensional image, their behavior under reference beam perturbation is different. This dynamic behavior, envisioned as a moving three-dimensional surface, provides information that allows the observer to remove the sign ambiguity and regain uniqueness. A formal uniqueness proof for fringe patterns originated by the holographic/hole-drilling technique is offered in Ref. 30.

The fringe-counting procedure described in this paper is valid as long as the grazing angle is $\gamma_1 < 90$ deg. When $\gamma_1 = 90$ deg, only out-of-plane displacements are picked up by the fringe pattern and the matrix of coefficients is singular in eq (21) since according to eqs (16)

$$K_x^0 = K_y^0 = 0$$

Moreover, the fringe counts between diametrically opposite points will always be zero since the phase shifts are $\phi(r, \theta) = \phi(r, \theta + \pi)$ due to the fact that $u_z(r, \theta) = u_z(r, \theta + \pi)$, i.e.,

$$\pi n^{(i)} = K_z u_z(r, \theta_i) = K_z u_z(r, \theta_i + \pi) = \pi n^{(i')}$$

A separate set of stress calculation formulas could be developed for this special case.

Finally, it is noted that alignment of the object with respect to the viewer or the illumination and reference beams is not important in this technique, only reasonably accurate measurement of optical parameters such as the grazing angle γ_1 is needed. The effect of surface topography may be another concern, but the holographic technique requires no special surface preparation and has been applied successfully to irregular surfaces such as those of weld beads,[31] which distorted fringe shapes to some extent but did not prevent an accurate fringe count. The technique can also be applied to curved surfaces as long as the curvature is such that the relations between stress and the displacements associated with hole drilling, derived for

an infinite plate, can be applied with sufficient accuracy. The same type of limitation is encountered in the strain-rosette technique.

Conclusions

There is sufficient displacement information contained in one holographic fringe pattern viewed in real time, made with a single beam and one direction of illumination, to uniquely determine principal residual stresses and their directions for uniaxial or biaxial stresses approximately uniform in the locale where a hole in introduced.

The fringe-counting method derived here allows stresses to be determined rapidly and with an accuracy comparable to other residual-stress measurement techniques.

The whole-field characteristics of a holographic fringe pattern allows one to recognize broadly the nature of residual stress present, e.g. uniaxial compression versus equibiaxial tension, and the relative magnitude of stresses, i.e., high, low, negligible.

Acknowledgments

The finite-element modeling in the present work was performed using a Cray YMP supercomputer running Abaqus v. 4.8.5 under academic license. The authors appreciate the CPU time granted by the San Diego Supercomputer Center. We are also grateful to Sandia National Laboratories for use of their experimental facilities and their support and help in conducting holographic-hole drilling tests.

References

1. *ASTM E837-89, "Standard Test Method for Determining Residual Stresses by the Hole-Drilling Strain-Gage Method," Annual Book of ASTM Standards, Section 3,* **03.01**, *713–718, Amer. Soc. for Test. and Mat., Philadelphia, PA (1989).*

2. *"Measurement of Residual Stresses by the Hole-Drilling Strain Gage Method," Technical Note TN-503-3, Measurements Group, Inc., Raleigh, NC (1988).*

3. *McDonach, A., McKelvie, J., MacKenzie, P., and Walker, C.A., "Improved Moiré Interferometry and Applications in Fracture Mechanics, Residual Stress and Damaged Composites," Exp. Tech.* **7** *(6), 20–24 (1983).*

4. *Nicoletto, G., "Theoretical Fringe Analysis for a Coherent Optics Method of Residual Stress Measurement," J. Strain Anal.* **23** *(4), 169–178 (1988).*

5. *Nicoletto, G., "Moiré Interferometry Determination of Residual Stresses in the Presence of Gradients,"* EXPERIMENTAL MECHANICS, **31** *(3), 252–256 (1991).*

6. *Furgiuele, F.M., Pagnotta, L., and Poggialini, A., "Measuring Residual Stresses by Hole-Drilling and Coherent Optics Techniques: A Numerical Calibration," J. Eng. Mat. Tech.* **113** *(1), 41–50 (1991).*

7. *Hung, Y.Y., and Hovanesian, J.D., "Fast Detection of Residual Stresses in an Industrial Environment by Thermoplastic-based Shearography," Proc. 1990 SEM Spring Conf. on Exp. Mech., Albuquerque, NM, 769–775, Society for Experimental Mechanics, Bethel, CT (1990).*

8. *Antonov, A.A., "Inspecting the Level of Residual Stresses in Welded Joints by Laser Interferometry," Weld Prod.,* **30** *(9), 29–31 (1983).*

9. *Bass, J.D., Schmitt, D., and Ahrens, T.J., "Holographic in situ Stress Measurements," Geophys. J. R. Astr. Soc.,* **85** *(1), 13–41 (1986).*

10. *Nelson, D.V., and McCrickerd, J.T., "Residual-Stress Determination Through Combined Use of Holographic Interferometry and Blind Hole Drilling,"* EXPERIMENTAL MECHANICS, **26** *(4), 371–378 (1986).*

11. *Smither, C.L., and Ahrens, T.J., "Displacements from Relief of In Situ Stress by a Cylindrical Hole," Int. J. Rock Mech. Min. Sci. & Geomech. Abstr.,* **28** *(2/3), 175–186 (1991).*

12. *Smither, C.L., Schmitt, D.R., and Ahrens, T.J., "Analysis and Modelling of Holographic Measurements of In Situ Stress," Int. J. Rock Mech. Min. Sci. & Geomech. Abstr.,* **25** *(6), 353–362 (1988).*

13. *Takemoto, S. (ed.), Laser Holography in Geophysics, Ellis Horwood, Chichester, England (1989).*

14. *Nelson, D.V., Fuchs, E.A., Makino, A., and Williams, D.R., "Residual-stress Determination by Single-axis Holographic Interferometry and Hole Drilling-Part II: Experiments,"* EXPERIMENTAL MECHANICS, **34** *(1), 79–88 (1994).*

15. *Kabiri, M., "Toward More Accurate Residual-stress Measurement by the Hole-drilling Method: Analysis of Relieved-strain Coefficients,"* EXPERIMENTAL MECHANICS, **26** *(1), 14–21 (1986).*

16. *Schajer, G.S., "Application of Finite Element Calculations to Residual Stress Measurements," J. Eng. Mat. Tech.,* **103** *(2), 157–163 (1981).*

17. *Ostrovsky, Yu., Shchepinov, V.P., and Yakovlev, V.V., Holographic Interferometry in Experimental Mechanics, Springer Verlag, Berlin (1991).*

18. *Vest, C., Holographic Interferometry, J. Wiley, New York (1979).*

19. *Stetson, K.A., "Fringe Interpretation for Hologram Interferometry of Rigid-Body Motions and Homogeneous Deformations," J. Opt. Soc. Am.,* **64** *(1), 1–10 (1974).*

20. *Nelson, D.V., "Determination of Residual Stresses by Single-Axis Holographic Interferometry and Blind Hole Drilling," Proc. 1990 SEM Spring Conference on Exp. Mech., Albuquerque, NM, 292–298, Society for Experimental Mechanics, Bethel, CT (1990).*

21. *Ennos, A.E., "Measurement of In-plane Surface Strain by Hologram Interferometry," J. Phys. E: Sci. Instrum., Series 2,* **1** *731–734 (1968).*

22. *Jones, R., and Wykes, C., Holographic and Speckle Interferometry, Cambridge University Press, Cambridge, England (1988).*

23. *Hariharan P., and Ramprasad, B.S., "Wavefront Tilter for Double-Exposure Holographic Interferometry," J. Phys. E: Sci. Instrum.,* **6** *(2), 173–175 (1973).*

24. *Plotkowski, P.D., Hung, Y.Y., Hovanesian, J.D., and Gerhart, G., "Improved Fringe Carrier Technique for Unambiguous Determination of Holographically Recorded Displacements," Opt. Eng.,* **24** *(5), 754–756 (1985).*

25. *Matthys, D.R., Dudderar, T.D., and Gilbert, J.A., "Automated Analysis of Holointerferograms for the Determination of Surface Displacement,"* EXPERIMENTAL MECHANICS, **28** *(1), 86–91 (1989).*

26. *Guo, Y., Post, D., and Czarnek, R., "The Magic of Carrier Fringes in Moiré Interferometry,"* EXPERIMENTAL MECHANICS, **29** *(1), 169–173 (1989).*

27. *Schajer, G.S., "Measurement of Non-Uniform Residual Stresses using the Hole-Drilling Method. Part I-Stress Calculation Procedures," J. Eng. Mat. Tech.,* **110** *(4), 338–343 (1988).*

28. *Nelson, D.V., Fuchs, E., Williams, D., and Makino, A., "Experimental Verification of the Single Axis Holographic Hole Drilling Technique," Proc. 1991 SEM Spring Conference on Exp. Mech., Milwaukee, WI, 293–300, Society for Experimental Mechanics, Bethel, CT (1991).*

29. *Holloway, D.C. and Durelli, A.J., "Interpretation of Fringes in Holographic Interferometry," Mech. Res. Comm.* **10** *(2), 97–103 (1983).*

30. *Makino, A., "Residual Stress Measurement Using the Holographic-Hole Drilling Technique," PhD Diss., Stanford University, Stanford, CA (1994).*

31. *Fuchs, E.A., Nelson, D.V., Mahin, K.W., and Williams, D.R., "Determination of Residual Stresses on and near Welds Using the Single Beam Holographic Hole Drilling Technique," Proc. 1991 SEM Spring Conference on Exp. Mech., Milwaukee, WI, 301–303, Society for Experimental Mechanics, Bethel, CT (1991).*